ORIGINAL PAPER

Mathematical insights into disassembly and separation of highly stressed CFRP structures

Janko Kreikemeier[1] · Hans Helge Schwieger[1]

Abstract

In the current effort towards sustainability, the aviation industry faces challenges in repurposing carbon fibre-reinforced plastic (CFRP) components effectively. Traditional "downcycling" methods fail to maintain CFRP integrity, as they involve cutting load-bearing fibres and re-embedding them with new polymers, which leads to fragmentation and loss of properties. Innovative solutions like non-destructive disassembly or dismantling offer precise separation without compromising fibre integrity. This method allows for the direct reuse of materials in similar or new applications and highlights the importance of advanced recycling technologies for fibre-reinforced plastics. In this work, an approach for disassembly based on the mechanism of wedge separation is developed. For this purpose, the mathematical fundamentals are first derived analytically and their applicability is demonstrated. Subsequently, the non-destructive disassembly of a stringer-stiffened CFRP structure is demonstrated using a Finite Element model in combination with a Cohesive Zone Approach. In summary, the wedge separation approach proves to be suitable for application in the non-destructive disassembly of stiffening elements, offering a promising method for future non-destructive disassembly within the scope of sustainable recycling.

Keywords Carbon fibre reinforced plastic (CFRP) · Non-destructive disassembly · Sustainable aviation · Wedge separation process · Advanced recycling technologies

List of symbols

Abbreviations

CFRP	Carbon fibre reinforced plastic
CZM	Cohesive zone model
DCB	Double cantilever beam
MFFD	Multi functional fuselage demonstrator
VCCT	Vertical crack closure technique

Latin letters

B	Bonded beam width [mm]
b_{wedge}	Width of wedge [mm]
c	Minimum crack length [mm]
E	Young's modulus [N/mm^2]
F_{crack}	Maximum load bearing capacity [N]
F_{gap}	Splitting vertical force component [N]
F_N	Normal force on inclined plane [N]
F_{R1}	Frictional force on inclined plane [N]
F_R2	Frictional force in x-direction [N]
F_{wedge}	Horizontal force on wedge element [N]
F_x	Balance force in x-direction [N]
F_y	Balance force in y-direction [N]
F_Y	Normal force in y-direction [N]
G	Energy release rate [N/mm]
G_{Ic}	Critical energy release rate [N/mm]
h_{wedge}	Height of wedge [mm]
I_y	Area moment of inertia [mm^4]
M_b	Bending moment [Nmm]
S_F	Safety factor [–]
t	Bonded beam height [mm]
U	Internally stored energy [Nmm]
W_b	Section moment [mm^3]

Greek letters

δ	Widening of the beam [mm]
γ	Wedge angle [–]
μ	Coefficient of friction [–]
σ_b	Maximum bending stress [N/mm^2]
$\sigma_{b,\,max}$	Maximum allowable bending stress [N/mm^2]

✉ Janko Kreikemeier
janko.kreikemeier@dlr.de

Hans Helge Schwieger
hans.schwieger@dlr.de

1 German Aerospace Center, Institute of Lightweight Systems, Lilienthalplatz 7, Braunschweig, Lower Saxony 38108, Germany

🙋 Springer

1 Introduction

The implementation of a separation process for CFRP structural components begins with the analysis of potential separation mechanisms. From the available fundamental principles, the most promising separation concept is selected. The primary objective of the separation method should be to detach the components without causing damage. To preliminarily verify this requirement, a simple analytical modelling of the separation method is performed. The results are then validated through a subsequent, more detailed FEM pre-investigation, reducing the risk of pursuing a non-functional process principle.

In analysing potential mechanisms, the process is oriented towards possible working principles, allowing for a mechanical, physical, or chemical primary process. Conventional machining separation methods per DIN 8580 [4] can be used for mechanical separation. Additionally, targeted material overload can exploit the most unfavourable peeling stresses on the bonding zone. Physical separation relies on heating the polymer material, while chemical processes use solvents to decompose the bonding zone. A comparison of these principles, with their respective advantages and disadvantages, is summarized in Table 1. Combinations of these principles are also feasible.

The main challenge in thermal and chemical separation is accessing the adhesive layer. To heat the adhesive through the surrounding components, only radiation heating or resistance heating is viable. Since CFRP has low penetration depths for laser beams [6], and inductive or resistance heating would heat the surrounding material equally, this method cannot be used for the unchanged base material. Similarly, the external application of solvents would damage surrounding components. However, if activatable elements like a heatable metal mesh or chemically activatable substances are integrated into the bonding zone, the adhesive can be selectively separated using these elements. The drawback is that only structures with these integrated mechanisms can be separated, and adhesive strength is likely reduced. Thus, a broader adhesive bond would be required, typically increasing the weight of the aircraft structure and leading to higher ecological costs during operation.

The combination of radiation heating and embedded metallic elements can be challenging to implement due to the existing lightning protection layer on the exterior, which is typically a metallic shield applied to the outer surface [8]. This layer would also absorb the radiation. In contrast, mechanical methods do not require pre-embedded mechanisms and can be applied to already manufactured structures. However, the structural components must allow sufficient access for a mechanism that induces material overload. A disadvantage is that the high process forces can lead to component damage. Weighing up the advantages and disadvantages, targeted mechanical material overload presents the greatest potential for the separation process, which is why this principle will be pursued further, Table 1. Nonetheless, separation using inductive heating and pre-embedded elements could be a viable alternative. For the mechanical overload of the adhesive, peeling of the components in Mode 1 or Mode 3, as illustrated in Fig. 1, is a viable option.

For Mode 1, applying force via a wedge between the elements is straightforward, as it simultaneously amplifies the required process forces and requires minimal space. Disassembly of structures similar to the MFFD benefits from low spatial requirements.

Table 1 Comparison of separation methods

Mechanical Separation		Physical Separation	Chemical Separation
Machining Processes	Deliberate Material Overload	Energy Dissipation	Decomposition
+ Low stress on base material + Well known process	+ No loss of material + Simple process	+ Complexly shaped adhesive surfaces are separable	
- Elaborate process technology - Cutting losses	- Possible component damage due to process forces - Complex adhesive forms are difficult to separate	- Only possible with a pre-inserted mechanism - Damage to surrounding structures due to heating/chemical effects - Lightning protection obstructive to radiant heating	
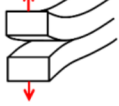
Fig. 1 Load modes of deliberate adhesive overload
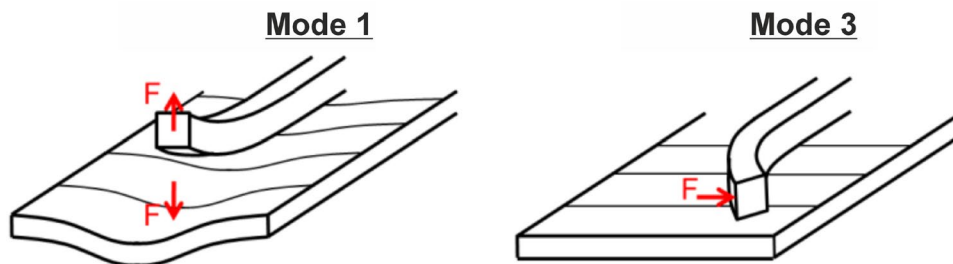
Demolition processes for such longitudinally and transversely stiffened structures should commence with the removal of continuous elements to avoid encircling the stiffeners with the separation mechanism. The tool must fit through the cutouts in the cross-bulkheads during removal, hence requiring minimal space. Additionally, Mode 1 is favoured due to the adhesive's lower strengths. However, its downside is the reduced load-bearing capacity of the thin outer skin vertically.

In Mode 2, however, the outer skin is loaded in a better orientation. A mechanism deforming the stiffener in the illustrated manner must either support itself on the shown stringer or remaining elements during disassembly. Both options are challenging to implement space-efficiently. For extensively protruding stringers, such as those with an omega cross-section, the stiffness of the stiffening element also poses a problem. Therefore, targeted mechanical overload focuses on Mode 1.

Before commencing the separation process modelling, estimating the most critical loading situation is possible. As each removed component reduces the overall stiffness of the structure during disassembly, the load-bearing effect of the stiffeners decreases. The outer skin becomes a vulnerable element in the process. As stiffness decreases, it becomes increasingly deformed, increasing the risk of breakage. Assessing whether the separation process is feasible with a wedge can thus occur during the removal of the last stiffening element. If the process analysis succeeds with this element, it's highly likely all preceding similar components can be removed using the wedge process. At the indicated critical stress point, the outer shell exhibits the lowest load-bearing capacity, Fig. 2.

The separation process with the wedge must thus proceed in two phases. In the first step, a crack is introduced into the undamaged adhesive layer at one end of the stiffener. In the second phase, this crack is extended along the longitudinal expansion of the stiffener with the splitting mechanism. Both process steps are necessary for the separation process to succeed. It is decided to analyse and realise the crack progression first in the test setup since, based on the initial assessment, it constitutes the more critical process segment. Therefore, it can be verified whether separation through targeted mechanical overload is fundamentally feasible.

2 Mathematical analysis of the wedge separation process

2.1 Analytical examination of wedge progression

The chosen wedge mechanism bears similarities to material separation in the DCB test, albeit aimed at relatively thin structural components. To generate an initial rough assessment of the process behaviour, the forces acting on the wedge are first analysed. Subsequently, based on the DCB models, a simplified analytical separation model is described.

2.1.1 Analysis of wedge forces

The force amplification of the wedge is derived through the force analysis of a simple frictional wedge model. The geometry depicted in Fig. 3 assumes the wedge's contact with the underside, exerting a splitting action on the peeled beam through the horizontal force F_{wedge}. Alternatively, a symmetric deformation of two equally stiff elements, pushed apart by the wedge, is conceivable. The following analysis aims to shed light on the theory of wedge separation.

The force balances in the horizontal and vertical directions yield

$$\sum F_x = F_{\text{R2}} + \cos(\gamma)F_{\text{R1}} - F_{\text{wedge}} + \sin(\gamma)F_{\text{N}} = 0, \tag{1}$$

$$\sum F_y = F_{\text{Y}} - \cos(\gamma)F_{\text{N}} + \sin(\gamma)F_{\text{R1}} = 0. \tag{2}$$

For the frictional forces, the assumptions apply

$$F_{\text{R1}} = \mu F_{\text{N}}, \tag{3}$$

$$F_{\text{R2}} = \mu F_{\text{Y}}, \tag{4}$$

which yields Eq. 5

$$F_{\text{N}} = \frac{F_{\text{wedge}}}{2\mu \cos(\gamma) - \mu^2 \sin(\gamma) + \sin(\gamma)}. \tag{5}$$

Fig. 2 Most critical load scenario at dissassembly
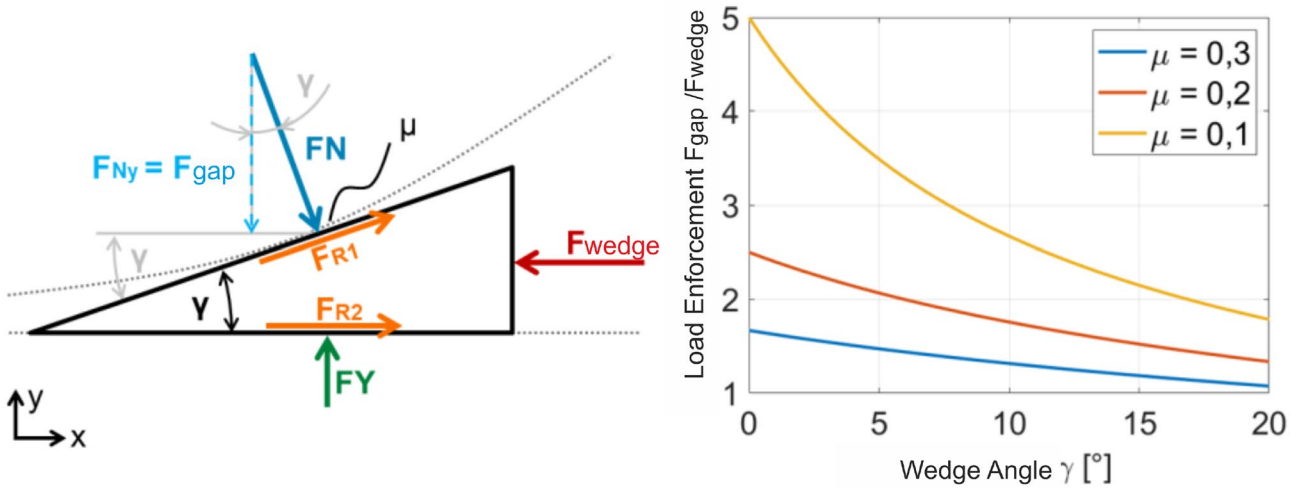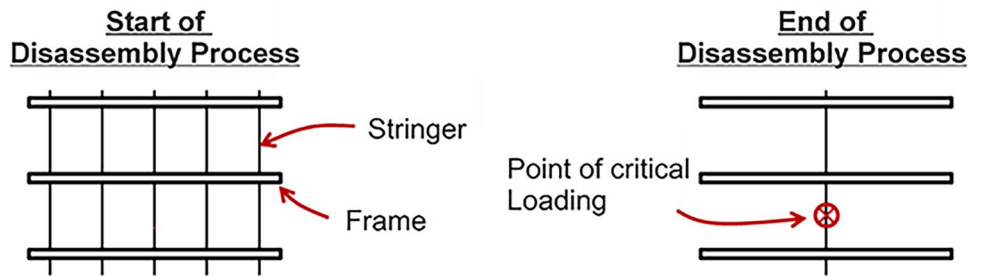
Fig. 3 Force amplification through wedge geometry
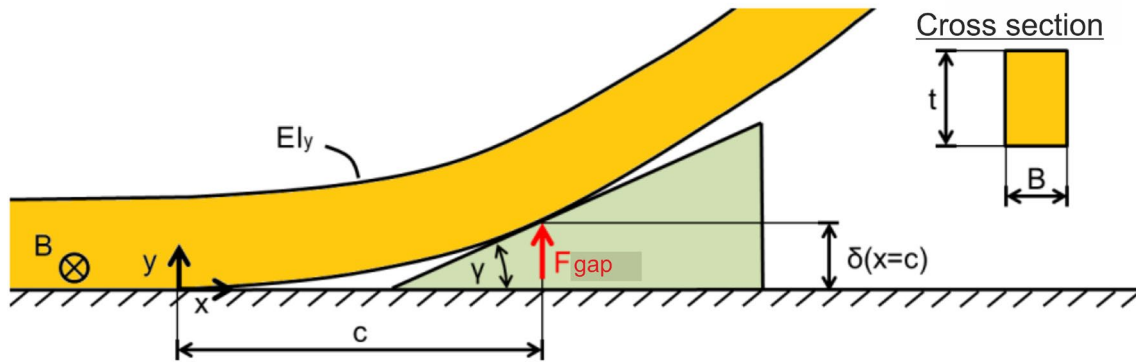
Fig. 4 Wedge model with rigid plate behaviour

The splitting vertical force component is determined by Eq. 6

$$F_{gap} = \cos(\gamma)F_N = \frac{F_{wedge}}{2\mu - \mu^2 \tan(\gamma) + \tan(\gamma)}. \qquad (6)$$

The relationship for the force amplification of the triggering force F_{wedge} from Eq. 6 is plotted on the right in Fig. 4. It can

be seen that an infinitely sharp wedge, with $\gamma \to 0°$, achieves a maximum force amplification of $1/(2\mu)$.

2.1.2 Model with rigid plate behaviour

In the analysis of the wedge process, the contact between the outer skin and the stiffening must be primarily

examined. At the beginning of the disassembly, the outer skin is stiffened by the surrounding stringers and transverse frames. As a first simple model behaviour, it can be assumed that the existing stiffeners fix the outer skin into an almost rigid state. From the consideration of energy release, analogous to the DCB (Double Cantilever Beam) test, a first simple crack model emerges. The energy release occurs exclusively from the stiffening element being detached. This can be modeled as an Euler bending beam with a fixed support at the crack tip. Crack propagation occurs when the critical energy release rate from the DCB test is reached. The resulting relationship is given by Eq. 7

$$G = -\frac{1}{B}\frac{\partial U}{\partial c} = -\frac{1}{B}\frac{\partial}{\partial c}\left(\frac{1}{2}F_{\text{gap}}\delta(x = c)\right) = \frac{1}{2B}\frac{F_{\text{gap}}^2 c^2}{EI_y} > G_{\text{Ic}}. \tag{7}$$

Here, G describes the energy release rate of the beam, U is the internally stored energy, B is the bonded beam width, and c is the length up to the bonded area, which corresponds to the crack length in the model. The geometric relationships are shown in Fig. 4.

The maximum energy is released when the beam is loaded with the maximum possible force F_{gap}. However, the splitting force can be limited by the maximum allowable load capacity of the components. From Eq. 7, a minimum crack length can thus be determined when the maximum allowable load capacity $F_{\text{gap}} = F_{\text{crack}}$ of the components is known, with the Eq. 8

$$c = \sqrt{\frac{2G_{\text{Ic}}BEI_y}{F_{\text{crack}}^2}}. \tag{8}$$

The corresponding widening of the beam and thus the minimum wedge thickness is determined according to the cantilever equation from [3] as

$$\delta(x = c) = \frac{F_{\text{crack}}c^3}{3EI_y}. \tag{9}$$

Since the wedge must lie exactly at the load point, it must be tangent to the deformation of the beam. The corresponding wedge angle can thus be calculated from the slope of the beam deformation, which is given by Eq. 10

$$\frac{\partial}{\partial c}\delta(x = c) = \frac{F_{\text{crack}}c^2}{EI_y}. \tag{10}$$

The corresponding wedge angle is then finally given by Eq. 11

$$\gamma = \tan^{-1}\left(\frac{\partial}{\partial c}\delta(x = c)\right) = \tan^{-1}\left(\frac{F_{\text{crack}}c^2}{EI_y}\right). \tag{11}$$

In this simple preliminary model, the crack length remains constant during the process. If the wedge is pushed further into the structure, the critical energy release rate is immediately exceeded, and the crack grows again to its initial size.

The maximum load-bearing capacity F_{crack} of the outer shell is initially difficult to estimate. However, the fracture of the beam element can be simplified and estimated through stress analysis of the bending stress. When considering the bonded structures, the stringer foot can be conceptually treated as a rectangular beam cross-section. The maximum acting bending stress in the outer fibre of a homogeneous beam material is determined according to [3] using the equation

$$\sigma_b = \frac{M_b}{W_b} = \frac{6F_{\text{crack}}c}{Bt^2}. \tag{12}$$

The maximum allowable bending stress $\sigma_{b,max}$ is reached by applying a safety factor S_F under the load of the fracture force, so that Eq. 12 can be transformed into

$$F_{\text{crack}} = \frac{Bt^2\sigma_{b,\max}}{6cS_F}. \tag{13}$$

If Eq. 13 is applied within the context of formula 8 and the moment of inertia for the rectangular beam cross-section according to [3] is included, the resulting relationship is obtained as follows:

$$c = \frac{\sqrt{6G_{\text{Ic}}ES_F}}{\sqrt{t\sigma_{b,\max}}}c. \tag{14}$$

in Eq. 14, the crack length can be eliminated, resulting in the final descriptive Eq. 15 as follows:

$$S_F = \sqrt{\frac{t\sigma_{b,\max}^2}{6G_{\text{Ic}}E}}. \tag{15}$$

Equation 15 integrates the considerations of the necessary released energy during crack propagation and the requirement for the non-destructive disassembly of the stringer foot. Interestingly, this equation is independent of the bonded beam width B and the crack length c. As shown above, the wedge forces decrease with increasing crack length; however, the lever arms increase correspondingly, so that the bending stress on the stiffener remains constant. Consequently, if the stringer foot represents the element at risk of fracture, any wedge thickness can be used according to the model behaviour, as long as an adequate safety factor according to the above Eq. 15 is met.

Table 2 Influence of stacking sequence in the rigid plate model

Stacking sequence	[45°,-45°,90°,0°,-45°,45°]s	12 x 0°	12 x 90°
Parameter	E = 48,4 GPa $\sigma_{b,max}$ = 318,1 MPa	E = 120 GPa $\sigma_{b,max}$ = 1200 MPa	E = 10,5 GPa $\sigma_{b,max}$ = 60 MPa
Equation 15	S_F = 1,715	S_F = 4,094	S_F = 0,6919
Result	Crack propagation occurs before the fracture of the stringer	Fracture risk is negligible; crack propagation occurs well before	Stiffening breaks before crack propagation becomes effective

Fig. 5 Stiffened shell structure on the Multifunctional Fuselage Demonstrator (MFFD), according to [5]

Illustratively, the result of Eq. 15 can be compared to a machining process. If a small chip thickness is removed in a figurative sense (value *t* is small and the equation is not satisfied), the chip tends to fracture into many small pieces due to the low moment of inertia. With large chip thicknesses (value *t* is large and the equation is satisfied), continuous chips form, appearing as long, peeled-off strips. The permissible bending load capacity of a heterogeneous beam with a given stacking sequence, Table 2, can be determined through layer-by-layer stress analysis and applied to the above equation.

In this model of rigid plate behaviour, in addition to neglecting the elasticity of the outer skin, several other simplifications are made. Shear stresses from the acting transverse forces, as well as interlaminar stresses, are neglected compared to the significantly higher bending stresses. Axial compressive stresses, predominantly caused by wedge friction, theoretically overlay the bending stress state at the wedge tip and further increase the safety factor. They are not considered in the simple model. Existing cracks can also lead to a deviation in the calculation. However, the model can serve as an initial rough and simple description of process behaviour and improved process understanding. A simplified design approach for the process and the theoretical limits can already be estimated from it.

The model is to be applied to the calculation of the stringer foot. According to Eq. 15, the stringer web does not represent a fracture-prone element, as the high underlying moment of inertia and the effectively large layer thickness conceptually increase fracture safety.

2.2 FEM application to a CFRP structure

Due to the complex geometries of the components, the existing layer construction, and the coupled deformation of the components, an improved analytical calculation is

Fig. 6 FEM model for stringer disassembly
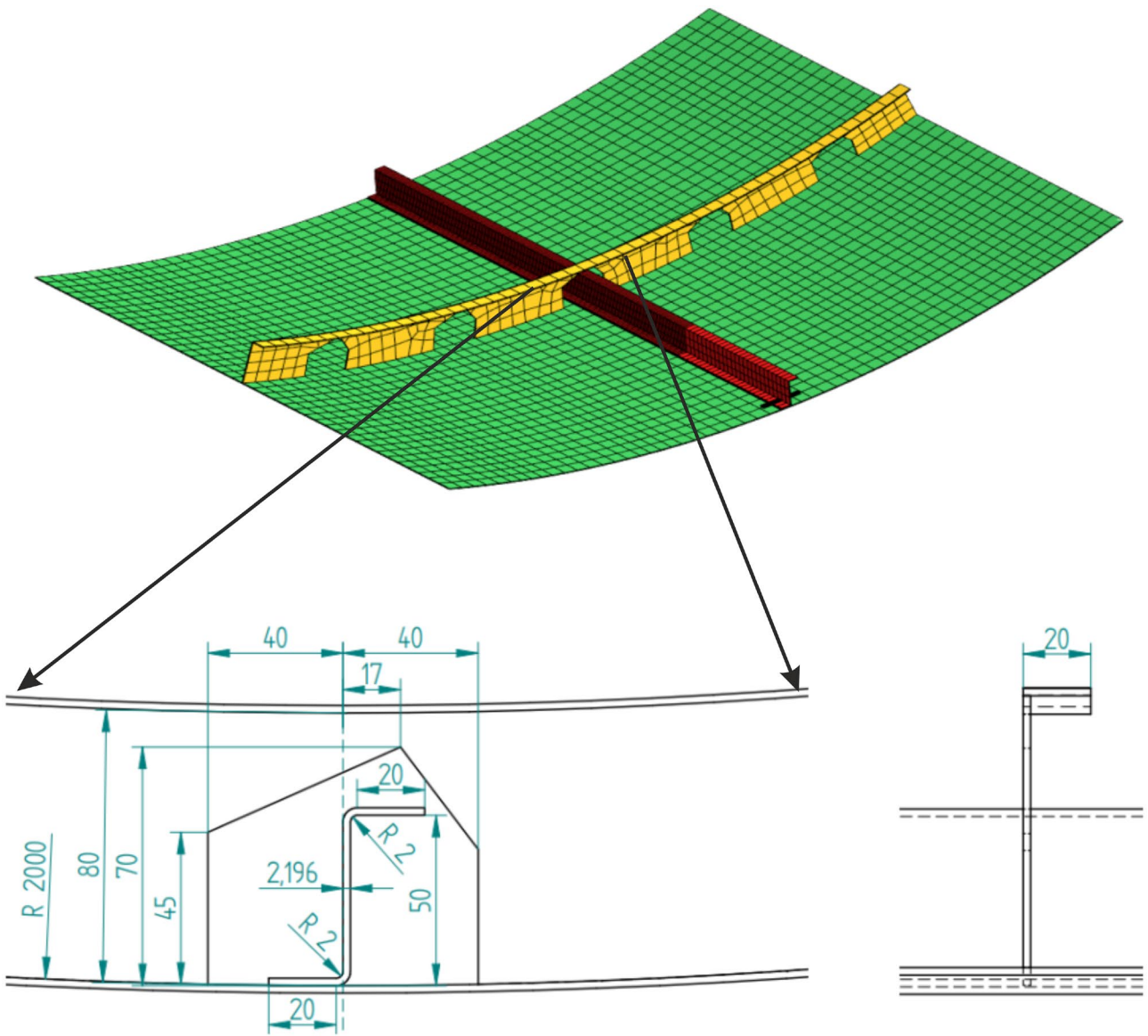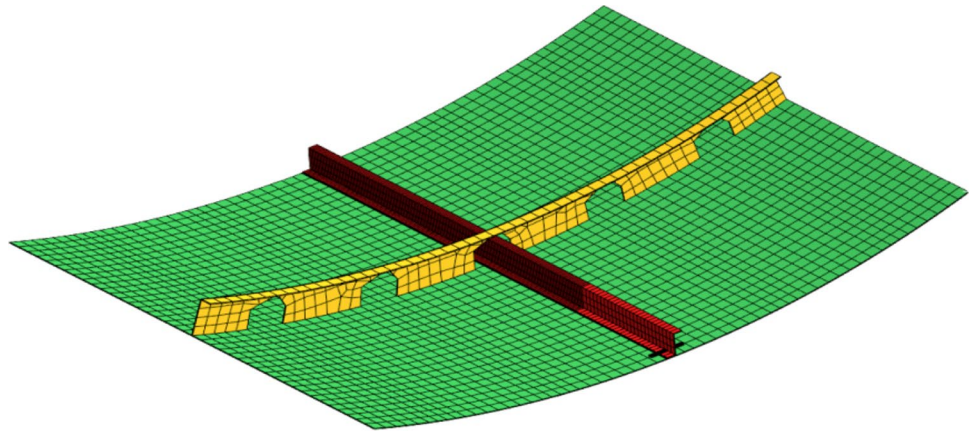
Fig. 7 Dimensions of CFRP structure

not easily achievable. However, these effects can be replicated in a FEM simulation. To assess whether the wedge process is generally suitable for damage-free separation of any structures before practical experimentation, such a FEM simulation is conducted on a sample model, as depicted in Fig. 5. The dimensions of the stiffened shell component were approximated based on the MFFD fuselage demonstrator and from Fig. 6. The chosen dimensions of the fuselage panel are depicted in Fig. 7. All components have the same material thickness of 2.196 mm due to the twelve-layer construction with a layer thickness of 0.183 mm. The stacking sequence defined is [45°, −45°, 90°, 0°, −45°, 45°]*s*, starting from the bottom layer.

2.2.1 Material definition

For the finite element investigations, ANSYS is utilized. In the test model, the separation of a stringer from the outer shell is to be analysed using a CZM approach. This simulation method allows for easy extension to investigate crack initiation behaviour and permits a wider range of contact materials compared to VCCT. For this initial investigation, an HTA/6376C combination is selected as the material combination, as both laminate properties and an associated cohesive zone model for the contact interface are available in the literature. The corresponding material parameters are given in Table 3, [7]. It is important to note for input into ANSYS that the contact stiffness *K* of the CZM model is not provided in the material data but is later defined in the "Model" module under contact properties. An additional damping coefficient for contact detachment is specified based on literature data. This stabilizes the highly nonlinear separation behaviour of the crack for the numerical solution calculation. Following [2], debonding is accompanied by convergence difficulties in the Newton–Raphson scheme. Therefore artificial damping is used in the numerical solution to overcome these issues. For the CFRP material data, the layer type must be specified as regular to apply the Puck failure criteria for laminate failure. The used wedge is modeled as an ideal linear elastic material for simplicity. To better simulate the subsequent

Table 3 Material and ply parameter of FEM model for stringer disassembly. The layer parameter data was extracted from [7]. For the failure parameters of the UD layer, the generally formulated data from [11] were used as a conservative estimate. The values were assumed to be slightly worse than in other more precise sources, such as [9]. The Puck parameters used were standard Ansys values similar to those specified in [11]. For the CZM model, data with experimental validation from [10], referencing critical energy release rates from [7], were utilized. The model was calibrated in [1] with VCCT

Simulation parameter—HTA 6367C		
Parameter	Symbol	Value
Unidirectional ply		
Young's modulus in fibre direction	$E_\parallel$	120,000 MPa
Young's modulus in transverse fibre direction	$E_\perp$	10,500 MPa
Shear modulus	$G_\parallel$	5250 MPa
Shear modulus	$G_\perp$	3480 MPa
Poisson's ratio	$\nu_\parallel$	0.3
Poisson's ratio	$\nu_\perp$	0.51
Failure parameter of unidirectional ply		
Tension strength in fibre direction	$R_{\parallel+}$	1800 MPa
Compression strength in fibre direction	$R_{\parallel-}$	1200 MPa
Tension strength in transverse fibre direction	$R_{\perp+}$	60 MPa
Compression strength in transverse fibre direction	$R_{\perp-}$	200 MPa
Shear strength in fibre direction	$R_{\parallel\perp}$	90 MPa
Shear strength in transverse fibre direction	$R_{\perp\parallel}$	77 MPa
Puck parameter		
Slope parameter—compression *XZ*	$\rho_{\perp\parallel-}$	0.3
Slope parameter—compression *YZ*	$\rho_{\perp\perp-}$	0.25
Slope parameter—tension *XZ*	$\rho_{\perp\parallel+}$	0.35
Slope parameter—tension *YZ*	$\rho_{\perp\perp+}$	0.25
CZM model parameter		
Critical energy release rate	G_{I_c}	0.26 N/mm
Max. contact stress	σ_{max}	30 MPa
Crack opening at bond rupture	δ_{max}	0.017 mm
Crack opening at max. contact stress	δ_0	3×10^{-6} mm
Contact stiffness	K	10^6 N/mm³
Artificial damping factor	AD	0.005 s

component deformation, an aluminum material is selected for the component under significant compressive load.

2.2.2 Geometry

The components are created using the Design Modeler integrated in ANSYS. The advantage of this is that the geometry parameters are directly incorporated and easily variable without transfer from another program. Additionally, the surface can be subdivided into partial surfaces within the module, simplifying the subsequent meshing process. For the model, the precise description of component stiffnesses is crucial. Since the available computational capacity is limited, only a portion of the outer skin can be replicated. The size of the cutout is determined by a preliminary study, the summary of which is depicted in Fig. 8.

In the preliminary investigation, the complete panel without cutouts in the transverse bulkheads is deformed by a high estimated point load of $F = 2000$ N at the critical loading point. A rapid mesh convergence study sets the element size to 25 mm, and subsequently, the panel width b is varied. As the width increases, the mid-span deflection converges to a constant value, reducing the influence of boundary conditions and deviations from real behaviour caused by them. Following this analysis, the entire panel width to be simulated is set to $b = 0.9$ m. This approach ensures an accurate description of the individual deformation behaviour of the outer skin regardless of the crack length. Additionally, the preliminary investigation reveals that the deformation of the outer skin is concentrated only on a section of the panel. The deformation behind the adjacent bulkheads is negligible. Due to this effect, it is decided to analyse the crack progression only over two-panel sections and to shorten the large panel, refer to Fig. 8 (left) for comparison with Fig. 10.

In addition to the plate geometry, the wedge geometry must be defined. In the rigid model behaviour shown in Fig. 5, a sharp wedge with flat sides tangential to the contact point is considered. Another possibility is a wire pulled through the material. The advantage of this would be that the geometry is tangential to the deformed surfaces regardless of curvature, ensuring a geometrically defined state. Additionally, the wire can adapt well to the multidimensional deformation of the plate. However, the disadvantage of a wire is the potential for high Hertzian pressures that could damage the component surfaces. Furthermore, evaluating the Hertzian pressure in the FEM model due to geometric nonlinearity would require a fine mesh resolution and
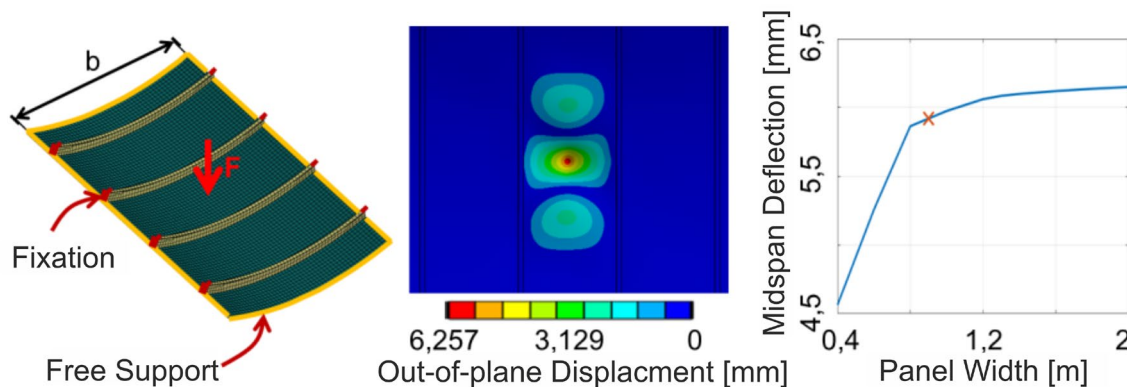
Fig. 8 Pre-model for investigation of disassembly process
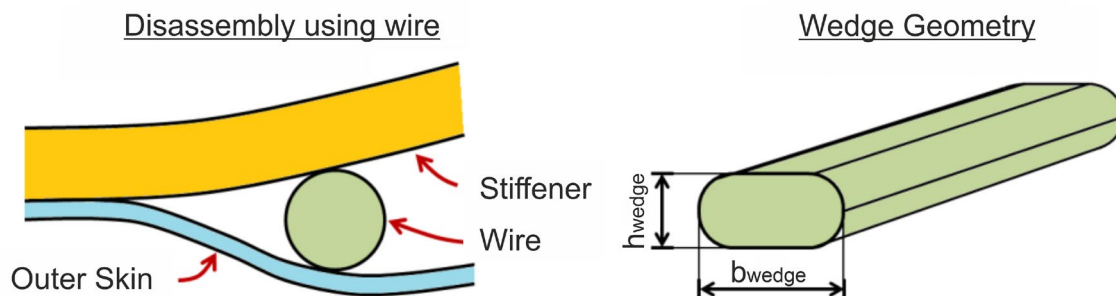
Fig. 9 Different wedge geometries
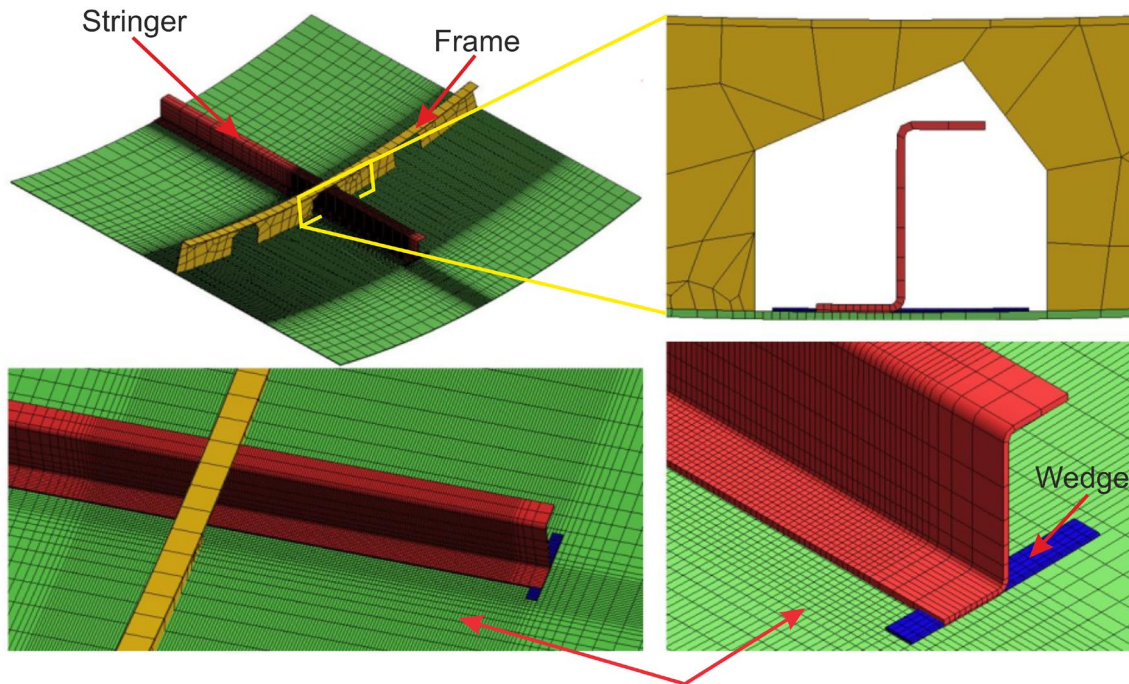
Fig. 10 Meshing of pre-model

consequently longer computation times. Therefore, to gain an initial understanding of the compressive loads, a rounded flat test wedge geometry is chosen, as shown in Fig. 9.

For the meshing of the component, Shell 281 elements in ANSYS are selected as the element type, as all the CFRP structures under consideration exhibit a low component thickness. This choice enables the laminate configurations to be processed using the ANSYS ACP pre-processor. The elements represent bending and membrane stresses, as well as shear force distributions. Quadratic shape functions are chosen, as they can represent continuous stress distributions. All components are generated with the same quasi-isotropic laminate configuration. Additionally, the meshing ensures uniform rectangular element shapes and smooth transitions in element sizes. The transverse rib and the edge regions are meshed relatively coarsely. In the area of the stringer-skin interface, the mesh is refined due to the cohesive zone model contact approach and the anticipated higher deformations and critical stress calculations. Based on a preliminary study, the mesh fineness in this region is set to 2 mm × 2 mm.

2.2.3 Analysis

In the ANSYS section "Tool", the relevant analysis settings are determined. This includes defining the contacts between the three components: stringer, wedge, and outer skin. For the CZM model, only the Pure Penalty method and the Augmented Lagrange method are suitable for contact detection. In the Pure Penalty method, when two components of the contact penetrate each other, a restraining spring-like force is introduced to counteract the penetration. In contrast, the Augmented Lagrange method increases the stiffness of the connection once a specific critical penetration is exceeded. Since the Pure Penalty method requires less computational time and the decisive factor is primarily the tensile action where the CZM model comes into effect, the Pure Penalty method is applied to all contacts. In the computational model, three different contacts are defined. The stringer is connected to the outer skin via a bonded "bounded" contact. The contact area extends up to the unrefined region, as shown in the bottom of Fig. 10. The unconnected remaining section represents an existing crack in the component. The bottom of the wedge is connected to the outer skin via a "no Separation" contact, ensuring it cannot detach from the surface. A third inserted "frictionless" contact acts between the top of the wedge and the stringer. This initial test model thus neglects frictional forces, as the friction parameters on the separate materials could only be roughly estimated, reducing the complexity of the model and the computation time. In the asymmetric contact algorithm in ANSYS, the penetration of the nodes of the "Contact" surface by the surface defined as "Target" is checked. It is recommended to define the softer or finer resolved material as "Contact" to avoid unwanted penetration of the more deformable material into the stiffer component. Therefore, the outer skin or the stringer is defined as "Contact" and the slightly coarser meshed wedge is defined as "Target". Additionally,

the "Shell Thickness Effect" is activated, which thickens the otherwise flat shell elements in the direction of the laminate thickness. From preliminary investigations, this variant has proven to be the only functional combination with the CZM modelling.

In addition to contacts, boundary conditions need to be defined. Analogous to Fig. 8, a roller support is used for the flexible bending outer skin. However, the reinforcing bulkhead is fixed at the ends. As shown in Fig. 10, it was decided not to replicate the adhesive bonding of the bulkheads in detail but to directly connect the associated nodes to the nodes of the outer skin.

The process can be simulated through a two-step approach as follows: In the first loading step, the existing crack is extended over the end of the stringer to slightly more than the required wedge thickness. The frictionless contact is deactivated during this step. In the second loading step, the contact is activated, the extension deformation is deactivated, and the leading edge of the wedge is pulled longitudinally under the stringer at a constant speed. The wedge moves completely through the refined area shown in Fig. 10. Within the boundaries of this area, the wedge surpasses the critical loading point and the reinforced section of the bulkhead, allowing for testing of the two assumed extreme states in the stiffness of the outer skin. The freedom of movement of the wedge in the vertical direction and rotation around the leading edge are allowed, while the remaining degrees of freedom are locked.

Finally, the solution algorithm settings are configured. It is important to enable the "Large Deflections" option. This accounts for geometric nonlinearity, considering membrane stresses generated in the deformed shell elements with increasing displacement. Initially, the wedge displacement is applied in 400 individual steps for the second loading step. Automatic variation of time steps with a high number of maximum time steps must be activated. Due to the large amount of data, it is advisable not to save every calculation step but to save only, for example, 200 data points.

2.3 Results

After 4000 iterations in the simulation and approximately 26 h of computation time for the 3 mm wedge, the output quantities of the model can be examined. The excerpt depicted in Fig. 11 illustrates exemplary results of the simulations on the 3 mm wedge at the position 120 mm before the stringer. In the figure, the fracture efforts corresponding to the inverse safety factors are color-coded. For better clarity, the red-colored wedge has been included in the figure. The color scale does not apply to this element.

During the wedge progression, three areas with higher loads become apparent. The highest fracture efforts occur during the travel at the artificially stiffened contact between the outer skin and the stringer. The loading effect of the stiffener, combined with the simplified geometry and the additional coarse meshing, create this unrealistic effect. The real stiffness here is significantly lower than in the model, leading to an underestimation of fracture safeties. For a detailed investigation, the bonding of the stringer should be accurately replicated. However, it can be suggested that the safety factors are well above 1.

The most realistically vulnerable area to fracture is the loading zone around the crack tip. The crack front curves with the extension of the stringer. Longer crack lengths
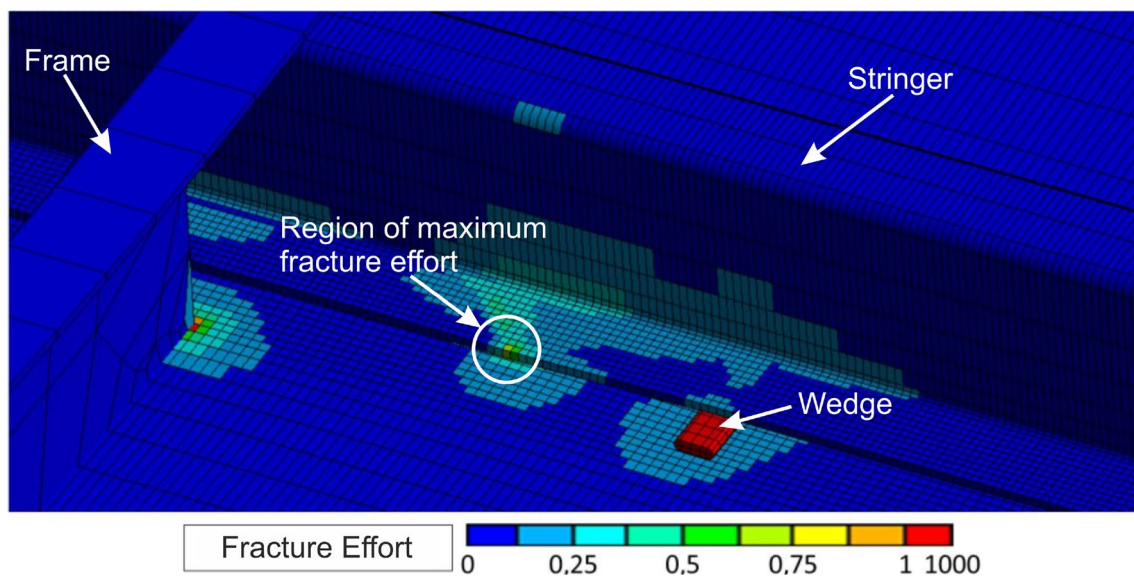
Fig. 11 Fracture effort of the pre-model

occur below the stringer flange than at the outer free edge. The result corresponds to the considerations of the simple analytical pre-model, where thicker laminate layers also generate longer crack lengths. As also suspected by the analytical model, the greatest fracture efforts occur at the outer free edge of the stringer. The supporting effect of the stringer flange decreases towards the edge. The stringer and the underlying outer skin show approximately the same fracture efforts with the risk of inter-fibre fracture. The third area with higher loads is around the contact zone between the wedge and the outer skin. However, the risk of fracture is significantly lower here than at the crack tip.

Depending on the simulated wedge thickness, the resulting fracture efforts and crack lengths vary during the wedge progression. However, the basic behaviour corresponds in both models to Fig. 11. For comparison of the effect of wedge thickness h_{wedge}, Fig. 12 depicts the fracture effort and crack length at the free end of the stringer foot. The wedge position at the passage through the stringer, as well as at the exceeding of the critical loading point, is marked in each case.

Up to approximately 15 mm of wedge displacement, the opening of the crack can be identified in the graphs. Subsequently, for the 1 mm thick wedge, there is a nearly constant behaviour in the fracture safeties, as well as in the crack lengths, which is somewhat independent of the wedge position and thus the stiffness of the plate. The graphs of the fracture safeties show larger fluctuations, which probably be explained by the inserted artificial damping effects, as well as by the contact stiffness of the "Pure Penalty" method. The safety factor for the 1 mm thick wedge, approximately $S_F \approx 1.9$, is slightly higher than the analytical calculation with $S_F \approx 1.7$ from Table 2.

In contrast to the thin wedge, with the thicker 3 mm wedge thickness, a clearer influence of the plate stiffness can be observed. The crack length increases until shortly before crossing the stringer. The large fluctuations in the graphs of the fracture safeties are unusual. Presumably, the solution is more strongly influenced by artificial damping. Since the crack opens at different speeds depending on the travel position, the artificial damping effects are inserted to different extents, leading to stronger fluctuations. This could also explain the significant change in fracture safety at the beginning of the simulation. The investigations and results presented here provide a foundation for further studies with more complex mathematical models. Future research should also be conducted to examine and evaluate the assumed rigidity of the plate and the influence of artificial damping in implicit calculations.

3 Conclusion and further work

The mathematical preliminary considerations, including FEM calculations, suggest that the wedge-based separation mechanism can be implemented without damaging the base material of the simulated shell structure. The safety margins observed in the analytical model are within an acceptable range, and the inclusion of additional damping forces, along with the neglect of friction coefficients, is theoretically expected to improve process safety. The study recommends using thinner wedges to minimize overall loads, reduce dependence on plate stiffness, and shorten crack lengths, thereby lowering the fracture risk. For thinner materials, weakening the adhesive properties, possibly through thermal processes, is proposed to facilitate separation without completely decomposing the adhesive zone. Overall, the wedge-based separation process appears promising for the non-destructive disassembly of stiffeners, offering the potential for a practical test stand.
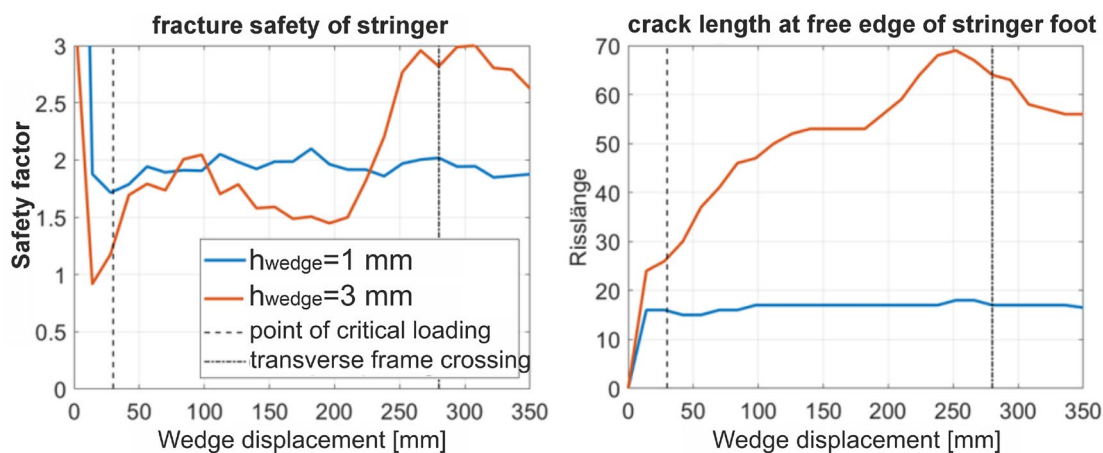
Fig. 12 Safety factors (left) and crack length (right). The dashed lines mark the points of critical loading, respectively, Fig. 3 (right)

To further advance dismantling as a sustainable technology, future research should focus on optimizing the wedge-based separation process for real-world applications. This includes refining the mathematical models to incorporate varying material properties and design complexities. Investigations into the influence of plate stiffness, friction, and damping forces in greater detail are necessary to enhance the process's robustness. Additionally, the development of mechanisms that can dynamically adjust to different material and structural configurations will be critical for scaling the technology. Future studies should also explore the integration of recyclability into the design phase, ensuring that components can be easily disassembled without damage. This novel approach can be referred to as Design-for-Disassembly. Further experimentation and prototype testing will be essential to validate the theoretical findings and establish practical guidelines for the implementation of dismantling technologies in the field of sustainable manufacturing and recycling.

Data availability Authors confirm that all relevant data are included in the article and/or its supplementary information files.

Declarations

Conflict of interest The authors declare that they have no conflict of interest. The corresponding author is also editor of this journal but was not involved in the review process of this paper.

References

1. Amiri-Rad, A., Mashayekhi, M., van der Meer, F.P.: Cohesive zone and level set method for simulation of high cycle fatigue delamination in composite materials. Compos. Struct. (2017). https://doi.org/10.1016/j.compstruct.2016.10.041

2. Ansys Inc.: 4.11. Cohesive Zone Material (CZM) Model. Ansys Inc., Canonsburg (2019). https://ansyshelp.ansys.com/account/secured?returnurl=/Views/Secured/corp/v194/ans_thry/thy_mat11.html.

3. Beitz, W., Küttner, K.-H.: Pocket Guide for Mechanical Engineering. Springer, Berlin (1981). https://doi.org/10.1007/978-3-662-29710-0 . (**in German**)

4. DIN 8580:2022-12, Terms, Classifications (12.2022): Manufacturing Processes. Norm 8580, Deutsches Institut für Normung e.V., 12 (2022) (**in German**)

5. Deutsches Zentrum für Luft- und Raumfahrt e.V. MFFD—Production Technology for the Thermoplastic Fuselage of Tomorrow (2022). https://www.dlr.de/zlp/desktopdefault.aspx/tabid-15354/27724_read-62324/#/gallery/38547

6. Hintze, W.: CFRP Processing: Separation Technologies for Composite Materials and Hybrid Lightweight Construction. Springer, Berlin (2021). (**in German**)

7. Johnson, W.S., Masters, J.E., Wilson, D.W., Juntti, M., Asp, L., Olsson, R.: Assessment of evaluation methods for the mixed-mode bending test. J. Compos. Technol. Res. (1999). https://doi.org/10.1520/CTR10611J

8. Karch, C., Metzner, C.: Lightning protection of carbon fibre reinforced plastics—an overview. In: Conference Paper, Munich, Germany, 11 (2017). Airbus Group Innovations. https://doi.org/10.1109/ICLP.2016.7791441. https://www.researchgate.net/publication/309231103_Lightning_Protection_of_Carbon_Fibre_Reinforced_Plastics_-_An_Overview_-.

9. Moure, M.M., Otero, F., García-Castillo, S.K., Sánchez-Sáez, S., Barbero, E., Barbero, E.J.: Damage evolution in open-hole laminated composite plates subjected to in-plane loads. Compos. Struct. (2015). https://doi.org/10.1016/j.compstruct.2015.08.045

10. Robinson, P., Galvanetto, U., Tumino, D., Bellucci, G., Violeau, D.: Numerical simulation of fatigue-driven delamination using interface elements. Int. J. Numer. Methods Eng. **63**, 1824–1848 (2005). https://doi.org/10.1002/nme.1338

11. Schürmann, H.: Designing with Fiber-Reinforced Composites. With 39 Tables. 2nd Revised and Expanded Edition. Springer, Berlin (2007)

Publisher's Note Springer Nature remains neutral with regard to jurisdictional claims in published maps and institutional affiliations.